Article

Direct growth of single-chiral-angle tungsten disulfide nanotubes using gold nanoparticle catalysts

Qinwei An [1] ✉, Wenqi Xiong [2,3], Feng Hu[4], Yikang Yu[5], Pengfei Lv[2], Siqi Hu[1], Xuetao Gan [1], Xiaobo He [6] & Jianlin Zhao [1] & Shengjun Yuan [2,3] ✉

Transition metal dichalcogenide (TMD) nanotubes offer a unique platform to explore the properties of TMD materials at the one-dimensional limit. Despite considerable efforts thus far, the direct growth of TMD nanotubes with controllable chirality remains challenging. Here we demonstrate the direct and facile growth of high-quality WS_2 and WSe_2 nanotubes on Si substrates using catalytic chemical vapour deposition with Au nanoparticles. The Au nanoparticles provide unique accommodation sites for the nucleation of WS_2 or WSe_2 shells on their surfaces and seed the subsequent growth of nanotubes. We find that the growth mode of nanotubes is sensitive to the temperature. With careful temperature control, we realize ~79% WS_2 nanotubes with single chiral angles, with a preference of 30° (~37%) and 0° (~12%). Moreover, we demonstrate how the geometric, electronic and optical properties of the synthesized WS_2 nanotubes can be modulated by the chirality. We anticipate that this approach using Au nanoparticles as catalysts will facilitate the growth of TMD nanotubes with controllable chirality and promote the study of their interesting properties and applications.

Quasi-one-dimensional (quasi-1D) van der Waals nanotubes, which can be viewed as cylinders rolled up from sheets of their two-dimensional (2D) counterparts, have opened new avenues for exploring physics in one dimension and building devices with unique functionalities[1,2]. As a prototypical example of 1D structure, TMD nanotubes (NTs) were discovered as early as 1992 (ref. 3), and they have received considerable attention due to their interesting physical properties, such as their enhanced intrinsic photovoltaic effect[4], superconductivity[5], diameter-dependent wetting[6], high strength, flexibility[7] and other emerging properties[8–10]. Up to now, TMD NTs, such as those of tungsten disulfide (WS_2), tungsten diselenide (WSe_2) and molybdenum disulfide

(MoS_2), have been mainly synthesized via a high-temperature solid–gas synthetic approach using metal oxide nanowhiskers as templates[11–15]. Despite its success in the synthesis of TMD NTs, this approach still suffers from poor controllability of the nucleation and growth process due to the multistep transformation of phases throughout the sulfurization of $WO_{3−x}$ ($MoO_{3−x}$) nanowhiskers. Moreover, while several studies on WS_2 NTs have shown that the wetting, superconductivity, exciton–polariton interactions and interlayer vibration modes strongly depend on their diameters[6,16–18], the effects of other geometric characteristics, such as the chiral angle, handedness and chirality, have not yet been reported. This is attributed to the fact that it is still a challenge to synthesize

[1]Key Laboratory of Light Field Manipulation and Information Acquisition, Ministry of Industry and Information Technology, Shaanxi Key Laboratory of Optical Information Technology and School of Physical Science and Technology, Northwestern Polytechnical University, Xi'an, China. [2]Key Laboratory of Artificial Micro- and Nano-structures of Ministry of Education and School of Physics and Technology, Wuhan University, Wuhan, China. [3]Wuhan Institute of Quantum Technology, Wuhan, China. [4]College of Materials Science and Technology, Nanjing University of Aeronautics and Astronautics, Nanjing, China. [5]School of Mechanical Engineering, Purdue University, West Lafayette, IN, USA. [6]Institute of Physics, Henan Academy of Sciences, Zhengzhou, China. ✉e-mail: anqw@nwpu.edu.cn; s.yuan@whu.edu.cn
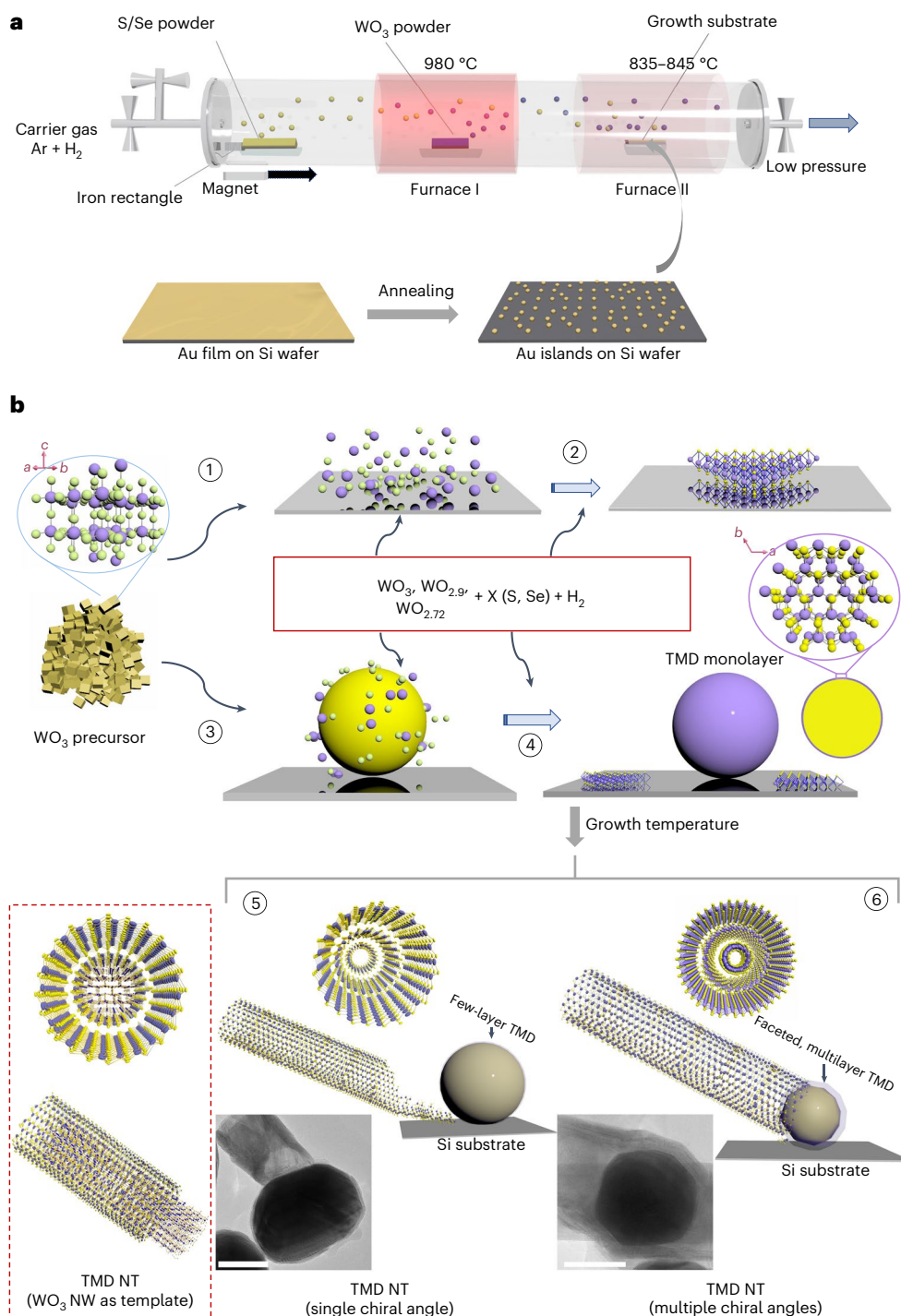
Fig. 1 | Direct CVD growth of TMD NTs using Au NPs as catalysts. a, Schematic illustration showing the preparation of the Au NP catalysts and the CVD growth of TMD NTs. **b**, Proposed growth mechanisms of TMD NTs. The standard 2D epitaxial growth of multilayer TMD crystals on the bare Si substrate follows steps 1–2, whereas the growth of TMD NTs due to the presence of Au NPs follows steps 3–4. There are two growth modes of TMD NTs depending on the growth temperature, that is, direct growth of 1D TMD NTs with a single chiral angle at

~835–840 °C (step 5) and with multiple chiral angles at ~840–845 °C (step 6). The insets in steps 5 and 6 are TEM images of TMD NTs with a single chiral angle and multiple chiral angles at their initial growth stages, exhibiting different nucleation sites and growth modes. The scale bars for the TEM images are 50 nm. The TMD NTs grown here are substantially different from the ones obtained by the high-temperature solid–gas synthetic approach using metal oxide nanowhiskers, which is presented in the dashed box.

TMD NTs with controllable chirality, which hinders further research in the field. Therefore, the synthesis of TMD NTs with high quality and controllable chirality is highly desired.

 Herein we report a direct growth of WS$_2$ NTs with controllable chirality using gold nanoparticles (NPs) as catalysts in a chemical

vapour deposition (CVD) process (Fig. 1a). We have observed that the Au NP catalyst provides unique accommodation sites for the reaction of the WO$_3$ vapour, hydrogen and sulfur, as well as the subsequent formation of WS$_2$ shells on the NPs' surface, which then seeds the growth of WS$_2$ NTs (Fig. 1b). This mechanism is entirely different from

the synthesis of WS$_2$ NTs by sulfurization of WO$_{3-x}$ nanowhiskers (Fig. 1b)[11,15]. Moreover, we reveal that the growth mode of NTs is sensitive to the temperature. Under the optimal growth temperature range, we achieve a yield of ~79% for WS$_2$ NTs that possess single chiral angles. This chiral-selective synthesis is also demonstrated in the WSe$_2$ NTs. TMD NTs with single chiral angles enable the study of chirality-related structural and physical properties, such as the geometrical character (faceting and helicity) and structural parameters, as well as optical and electronic properties.

Direct growth of TMD NTs

The direct growth process of WS$_2$ and WSe$_2$ NTs using gold NP catalysts is schematically illustrated in Fig. 1a. The Au NPs are firstly obtained by annealing an ~10 nm Au film deposited on a Si substrate at 750 °C for 10 min (Supplementary Fig. 2a,b) and then placed in the middle of furnace II. During the synthesis, WO$_3$ powders, as the source materials, are located in the middle of furnace I and are evaporated by increasing their temperature; the vapour is transported onto the Si substrate by Ar gas flow. When the temperatures in furnaces I and II simultaneously reach the required values (920 °C and ~835–845 °C, respectively, as shown in Supplementary Fig. 2c), hydrogen gas is injected, and the S or Se powders are quickly moved to furnace I by moving the iron rectangle behind the boat by a magnet. As a result, the S or Se powders in the boat start to evaporate and react with the WO$_3$ layer formed on the surface of the Au NPs, ultimately transforming WO$_3$ into a WS$_2$ or WSe$_2$ monolayer.

The growth of the TMD nanocrystals on the Si substrate, without or with Au NPs, is comparatively illustrated in Fig. 1b (steps 1 → 2 and steps 3 → 4, respectively). In the absence of Au NPs, the nucleation of WO$_{3-x}$ (step 1, Fig. 1b) and growth of WS$_2$ (step 2, Fig. 1b) are thermodynamically favourable on the bare Si substrate, resulting in 2D epitaxial growth (Supplementary Fig. 3a,b) and island growth (Supplementary Fig. 3c,d) dominated by the Frank–van der Merwe growth mode and Stranski–Krastanov growth mode, respectively[19,20]. By comparison, the presence of the Au NPs provides accommodation sites for the WO$_3$ and S/Se vapours, and induces the nucleation of a WO$_3$ crystalline layer on the surface of the NPs (step 3, Fig. 1b), followed by the formation of a TMD monolayer (step 4, Fig. 1b).

Our studies further reveal that the growth process of NTs is highly sensitive to the temperature of the substrate (Supplementary Fig. 4). The temperature influences the nucleation sites of NTs, either at the edge contact between the NPs and Si substrate, or on the surface of the catalyst NPs (step 5 or 6 in Fig. 1b and Supplementary Fig. 4b,c), leading to the growth of NTs with a single chiral angle or multiple chiral angles, respectively. Two types of growth modes will be discussed in detail in the following. The influence of prematurely introducing the S vapours into the furnace are also studied (Supplementary Fig. 5). Additionally, Supplementary Fig. 6 illustrates the feasibility of the step-by-step catalytic CVD reaction in a tubular furnace with a single temperature zone.

The scanning electron microscopy (SEM) measurements confirm that WS$_2$ NTs can be effectively obtained on the Si substrate (Fig. 2a). The Au catalyst NPs on the growth substrate are located at the root of the synthesized WS$_2$ NTs and assist the growth of the NTs. Figure 2b displays the low-resolution transmission electron microscopy (TEM) images of the WS$_2$ NTs grown at ~835–840 °C, revealing representative tubular structures. The selected-area electron diffraction (SAED) of WS$_2$ NTs (inset of Fig. 2b) consists of a single set of hexagonally arranged diffraction patterns, indicating an identical helical angle for all concentric shells in the multi-walled NTs. For two special cases in WS$_2$ NTs, the armchair-type or zigzag-type WS$_2$ NTs have chiral angles of 0° and 30°, respectively, exhibiting only one set of hexagonal spots in reciprocal space (Supplementary Section 1). It is clear that the WS$_2$ NT is a zigzag-type WS$_2$ NT[21,22]. Their high-resolution TEM images further confirm high-quality multi-walled NT structures with interlayer spacings of 0.634 nm (Fig. 2c) and a periodic honeycomb structure in the middle of the NT.

The atomic structures and chemical compositions of the as-synthesized WS$_2$ NTs are uncovered by aberration-corrected scanning transmission electron microscopy–annular dark-field (STEM-ADF) imaging and energy dispersive X-ray spectroscopy (EDS) studies. The NTs grown at ~835–840 °C (Fig. 2d) present the atomic columns of S–W–S chevrons along the [001] direction at the edge of the NTs, matching the rhombohedral symmetry (3R) phase of WS$_2$ (refs. 23,24), as overlaid and aligned with the atomic structure model. Further X-ray diffraction studies and SAED patterns of the WS$_2$ NTs also confirm the 3R phase[23], which is distinct from the hexagonal (2H) phase of the few layers of WS$_2$ (Supplementary Fig. 7) and the WS$_2$ NTs grown from W$_{18}$O$_{49}$ nanowhiskers[11]. The atomic arrangement in the middle of the NTs displays a periodic honeycomb structure along the [001] direction. The atomically resolved STEM images and intensity profiles in the middle of the NTs are consistent with simulated ones for multilayer WS$_2$. These results indicate that all cylindrical layers in WS$_2$ NTs should have the same chiral angle. EDS measurements are carried out for the as-synthesized single-chiral-angle (S-CA) NTs (Supplementary Figs. 8 and 9).

At ~840–845 °C, the as-synthesized NTs exhibit distinct morphologies and nucleation sites (Fig. 2e) compared with the NTs grown at ~835–840 °C, implying different growth modes. Figure 2f displays the low-resolution TEM images of the synthesized WS$_2$, revealing a similar representative tubular structure. However, the SAED of the NTs grown at ~840–845 °C (inset of Fig. 2f) have two groups (four sets) of hexagonal diffraction spots, demonstrating multiple-chiral-angle (M-CA) characteristics with helical angles of 8.5° and 20.5°. This characteristic leads to a moiré superlattice atomic arrangement in the multi-walled NTs, as shown in the inset of Fig. 2g. Our further analysis based on the STEM-ADF imaging provides more details on the atomic arrangement and chemical compositions of the NTs (Fig. 2h). The characterization of the twist can be directly visualized by the stacking order of the S–W–S chevrons at the edge of the NT. This is consistent with the twisted atomic models depicted in Supplementary Fig. 10. The STEM image in the middle of the NTs reveals a resolved moiré superlattice. The red arrows indicate the smallest periodic repeating cell, with a lattice constant of 1.51 nm. This mostly agrees with the simulated atomic structure model of multilayer WS$_2$ with 12.1° twisted angles, which displays a moiré superlattice with a moiré periodicity of 1.50 nm. The EDS elemental mappings of the M-CA NTs are shown in Supplementary Figs. 11 and 12.

To verify the temperature-dependent chiral characteristics of the synthesized WS$_2$ NTs, we randomly selected and characterized approximately four hundred NTs grown at ~835–840 °C or ~840–845 °C. At ~835–840 °C, nearly 79% of the as-grown NTs we synthesized possess single chiral angles (Fig. 2i, Supplementary Fig. 13 and Supplementary Table 1). Notably, most of the S-CA WS$_2$ NTs have armchair or zigzag configurations, consistent with the reported results of carbon NTs[25] and other van der Waals NTs[1]. At ~840–845 °C, 88% of the synthesized WS$_2$ NTs have at least three chiral angles (Fig. 2j and Supplementary Fig. 14), and only a small percentage (5.6%) of the NTs have a single helical angle. Our further investigations indicate a similar influence of growth temperature on the chiral character of synthesized WSe$_2$ NTs (Supplementary Figs. 15 and 16), with a similar selectivity for chiral angles 30° and 0° (also Supplementary Table 2). Interestingly, our results are consistent with the observation in multi-walled carbon NTs, where the growth at a lower temperature typically leads to S-CA multi-walled carbon NTs[26,27], suggesting a general effect of the growth temperature on the growth of inorganic multi-walled NTs.

Growth mechanism and dynamics

Figure 3a shows a TEM image and EDS analysis of an Au NP, confirming that the Au NPs, with a pure chemical composition of Au, are not perfect spheres. The high-resolution TEM image reveals lattice fringes with an average spacing of 0.230 nm, matching well with the (111) plane
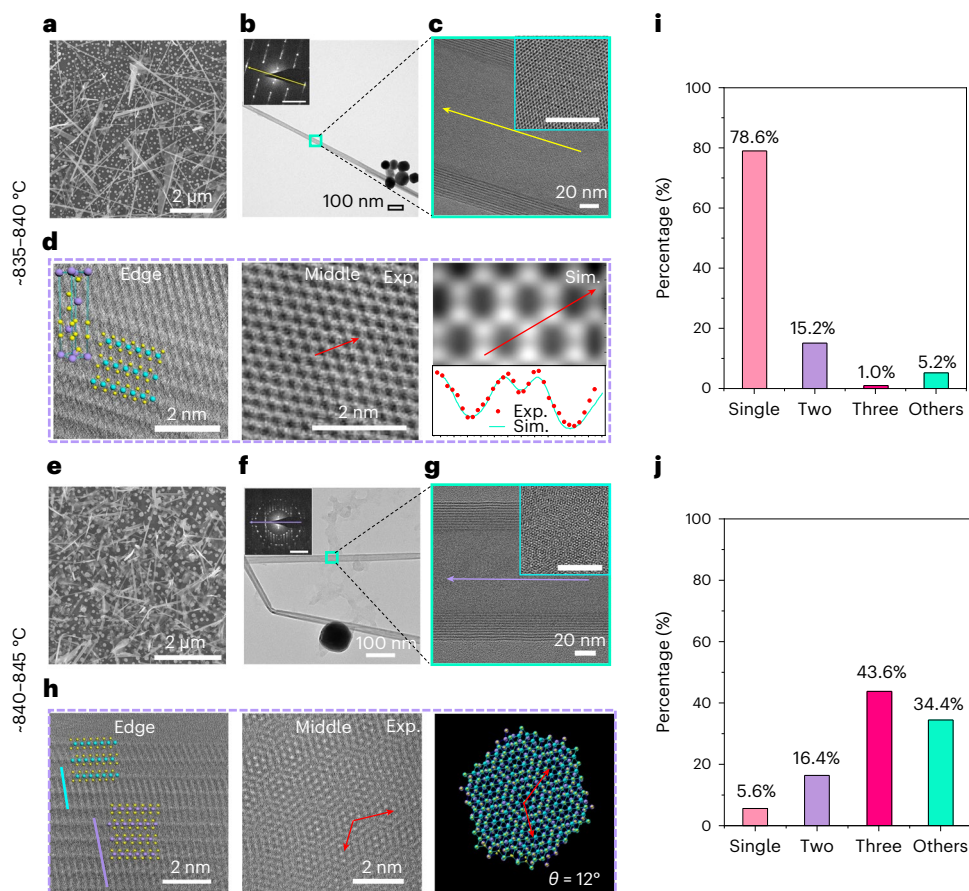
Fig. 2 | Structural characterizations of WS₂ NTs grown at different growth temperatures. a–c, SEM (**a**), TEM (**b**) and high-resolution TEM (**c**) of the WS₂ NTs grown at ~835–840 °C. The inset in **b** displays the corresponding SAED pattern of the NT; **c** shows a zoomed-in view of **b**; and the inset in **c** is a zoomed-in view at the middle region of the NT, with a scale bar of 20 nm. **d**, Experimental (Exp.) and simulated (Sim.) STEM(-ADF) images and intensity profiles of a WS₂ NT grown at ~835–840 °C. The stacking order of the S–W–S chevrons at the NT edge displays the characteristic arrangement of the rhombohedral symmetry (3R) phase, as overlaid and aligned with the atomic structure model where the W atoms are coloured turquoise, and the S atoms are yellow. Intensity profiles are obtained along the red arrows marked in the experimental and simulated STEM

images. **e–g**, SEM (**e**), TEM (**f**) and high-resolution TEM (**g**) of the WS₂ NTs grown at ~840–845 °C. The inset in **f** displays the corresponding SAED pattern of the NT; **g** shows a zoomed-in view of **f**; and the inset in **g** is a zoomed-in view at the middle region of the NT, with a scale bar of 20 nm. **h**, STEM-ADF images at the edge and middle of a WS₂ NT grown at ~840–845 °C, and the modelled atomic structure of a WS₂ bilayer with a twist angle of 12°. The lattice vectors of the moiré superlattice are highlighted by red arrows. The colours in the atomic structure model are the same as in **d. i,j**, Histograms of the distribution of the synthesized WS₂ NTs with different chiral angles for growth temperatures of ~835–840 °C and ~840–845 °C, respectively.

of the Au face-centred cubic (fcc) structure[28,29]. With the evaporation of WO₃ powder, a WO₃ shell with a thickness of 2–3 nm is formed on the surface of the Au NPs (Fig. 3b). Additionally, the measurements of the lattice fringes, EDS mapping (inset of Fig. 3b) and quantitative analysis of the element ratios of the core–shell structures (Supplementary Fig. 17) are presented.

Following the evaporation of S powder, the WO₃ crystalline layer undergoes a reaction with the S atoms, resulting in the appearance of a disordered structure on the surface of the WO₃ crystalline layer (Supplementary Fig. 18). This disordered state indicates a phase transformation and the formation of the WO₃₋ₓ suboxides, which plays a crucial role in the initial formation of a WS₂ crystalline monolayer (Supplementary Figs. 19 and 20). As a result, the WO₃ crystalline shell eventually converts into WS₂, forming a monolayer on the surface of the Au NPs (Fig. 3c), which effectively seeds the subsequent growth of two types of WS₂ NTs, depending on the growth temperature.

At the growth temperature of ~835–840 °C, the growth of WS₂ NTs is dictated mainly by edge energetics[30,31]. With the rapid addition of the S and W atoms to the growth front, the few layers of WS₂ formed on the Au NPs extend and induce the formation of WS₂ layers on the Si

substrate (Fig. 3d(i) and Supplementary Figs. 21 and 22). The interface between the WS₂ layer on the surface of the Au NPs and the one on the Si substrate provides preferential nucleation sites for the further growth of WS₂ vertical flakes (Fig. 3d(ii,iii) and Supplementary Fig. 23a). As a WS₂ flake grows and extends further, the built-in strain (surface tension) within each layer increases rapidly, inducing a spontaneous rolling-up process[32,33] and leading to the formation of a WS₂ nanoscroll, with a single or few walls (Fig. 3d(iv)). The nanoscroll becomes a base structure for further layer-by-layer growth. Eventually, a multi-walled WS₂ NT with a length of a few micrometres is formed, and the helical angle of each layer remains the same (Fig. 3d(v) and Supplementary Fig. 23). The TEM image of the resulting WS₂ NT, shown in Fig. 3d(vi), confirms the interface growth mode.

By contrast, at ~840–845 °C, the WS₂ monolayer formed on Au NPs serves as a seed for continuous homoepitaxial layer-by-layer growth (Fig. 3e(i,ii) and Supplementary Fig. 24)[34,35]. The formation of the WS₂ layer shell results in a remarkable reconstruction of the Au NPs, transforming them from an irregular sphere to a polyhedron with a hexagonal cross-section, known as polyhedral faceting. Meanwhile, the WS₂ layers stacked on Au NPs can extend outwards from the corner of
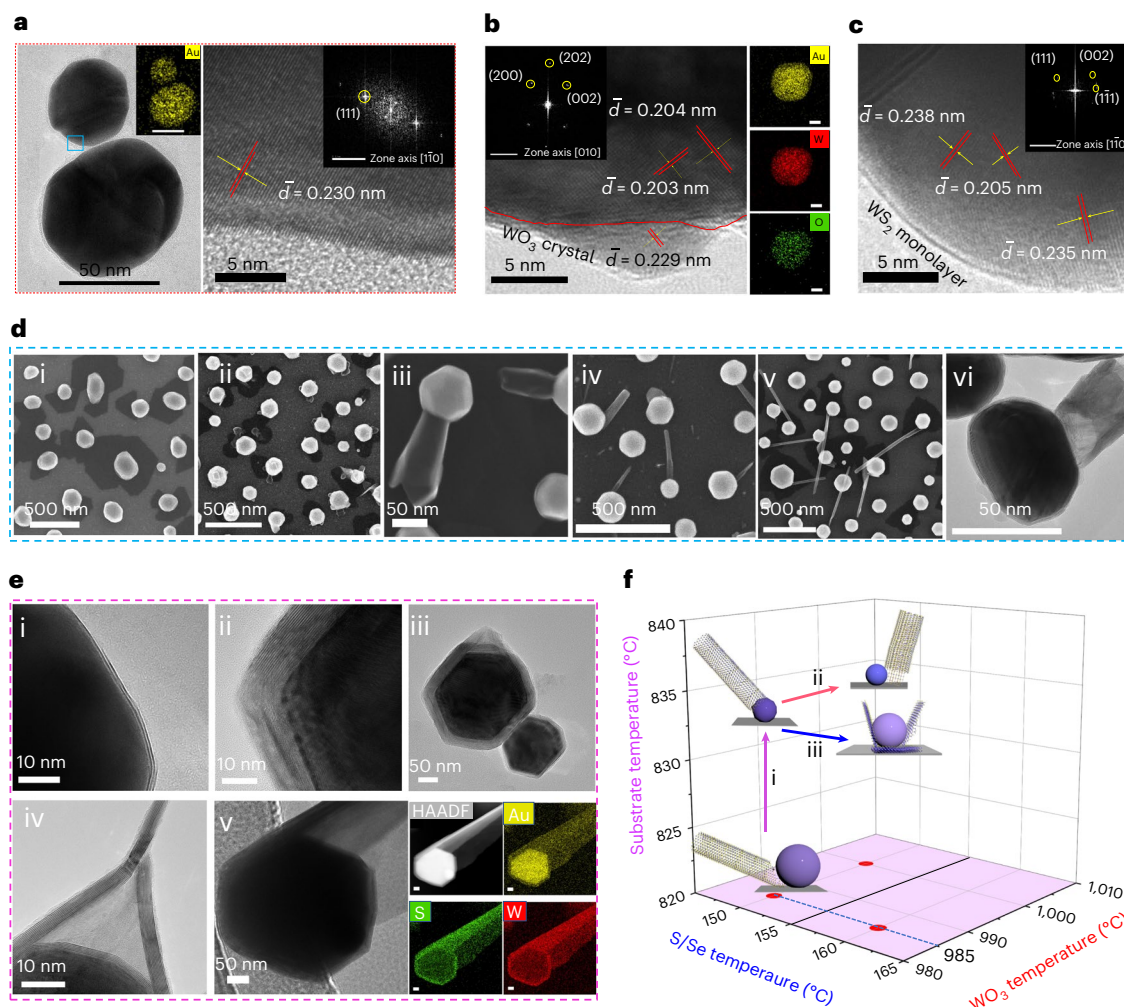
Fig. 3 | Growth mechanism and dynamics of WS$_2$ NTs catalysed by Au NPs.
a, TEM image of Au NPs with EDS mapping in the inset (left). High-resolution TEM image with corresponding fast Fourier transform pattern in the inset (right). **b**, TEM image of structures at the initial stage of NT growth, where the WO$_3$ crystalline shell is formed on the surface of Au NPs. Left inset shows the fast Fourier transform pattern, and right inset shows the EDS mappings. $\bar{d}$, the average spacing of lattice fringes. **c**, TEM image and corresponding fast Fourier transform (inset) of the Au NPs' surface after the reaction with S atoms. The previously formed WO$_3$ crystals are transformed into a WS$_2$ monolayer on the surface of Au NPs. **d**, SEM images showing the growth process of WS$_2$ nanostructures at ~835–840 °C (i–v). The few layers of WS$_2$ formed on the Au NPs extend and induce the formation of WS$_2$ layers on the Si substrate; thus,

the interface between the WS$_2$ layer on the Si substrate and the WS$_2$ shell on the surface of the Au NPs provides preferential nucleation sites for the growth of NTs. The TEM image of the resulting WS$_2$ NT is shown in (vi). **e**, TEM images of Au NP–WS$_2$ shell heterostructures at ~840–845 °C. The continuous homoepitaxial layer-by-layer growth on the WS$_2$ monolayer leads to the polyhedral faceting of the Au NP and the formation of a seamless multi-walled NT with different helicity. At the bottom right is the EDS mapping. HAADF, high-angle ADF. **f**, A phase diagram showing influences of the temperatures of the substrate, WO$_3$ and S/Se powders on the growth of WS$_2$ nanostructures. The growth of WS$_2$ NTs based on the formed WO$_{3-x}$ nanowires with considerable vapour pressure of WO$_3$ is shown (ii), as well as the development of the vertical WS$_2$ nanosheets with considerable vapour pressure of S (iii).

the hexagonal cross-section, supporting the extension growth of the WS$_2$ shells (Fig. 3e(iii,iv) and Supplementary Fig. 25). Considering the three-dimensional (3D) character of the heterostructures composed by the faceted Au NP core and WS$_2$ layered shells, there could be extensive growth of WS$_2$ simultaneously along the tangential direction of the corner and around the circumference (Fig. 3e(v)). As a result, a seamless NT with multiple walls but different helicity is formed, as confirmed by the SAED measurements (Supplementary Figs. 26 and 27).

Our observations suggest that at temperatures of ~835–840 °C, the growth is dominated by the interface energetics, and the development of WS$_2$ NTs follows an interface growth mode. By contrast, at temperatures of ~840–845 °C, it is energetically more favourable to lower the surface energy by forming a thicker shell on the Au NP, leading to a surface growth mode. Our further studies show that a similar mechanism appears in the growth of WSe$_2$ NTs, where the interface and

surface growth modes are dominant at ~835–840 °C and ~840–845 °C, respectively (Supplementary Figs. 28 and 29). We conduct further analysis to study the effect of the vapour pressure of WO$_3$ and S on the formation of WS$_2$ NTs (Supplementary Fig. 30–33) and summarize these results as a growth phase diagram, which is plotted in Fig. 3f. In addition, the non-uniform distribution of Au NPs and uncontrolled nucleation of WO$_3$ or WO$_{3-x}$ crystals on the growth modes are discussed (Supplementary Fig. 33).

Structural correlation, helicity and faceting analysis

For multi-walled WS$_2$ NTs with a single chiral angle, the interlayer spacing shrinks approximately linearly when increasing the layer number, with the rate of shrinkage dependent on the chiral angle (Fig. 4a and Supplementary Figs. 34 and 35a). When increasing the outermost
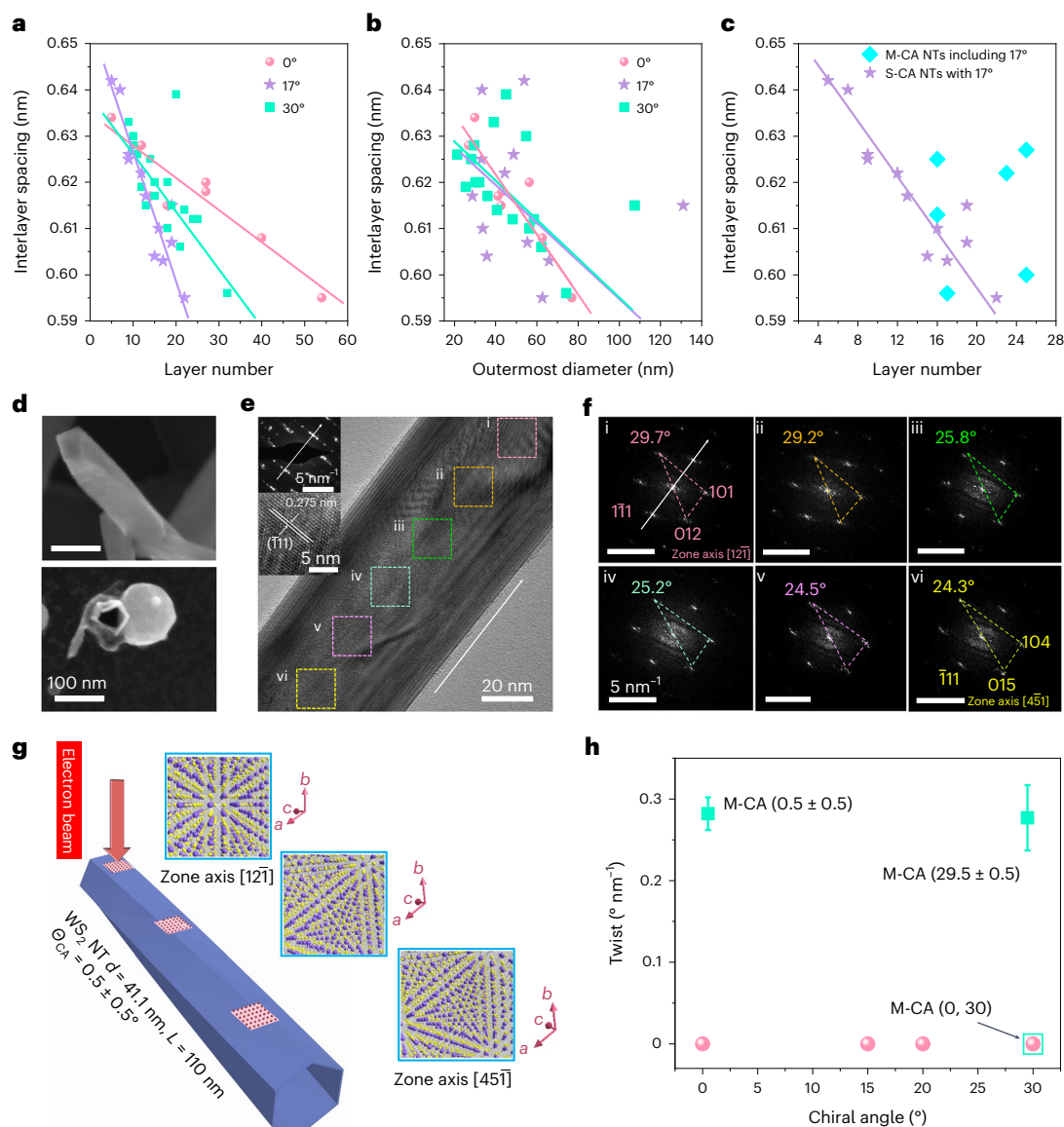
Fig. 4 | Correlation of the structural parameters, helicity and faceting of the WS₂ NTs. a,b, The interlayer spacing as a function of layer number (**a**) or the outermost diameter (**b**) for the armchair, zigzag and chiral WS₂ NTs with angles of $17 \pm 0.5°$. **c**, The interlayer spacing as a function of layer number in S-CA WS₂ NTs with chiral angles of $17 \pm 0.5°$, compared with M-CA WS₂ NTs including similar chiral angles ($17 \pm 0.5°$). **d**, SEM images of multi-walled WS₂ NTs with a vertical growth direction. **e**, TEM image of a M-CA WS₂ multi-walled NT with chiral angles distributed within $0.5 \pm 0.5°$. The insets show the corresponding SAED pattern and lattice fringes of ($\bar{1}11$) planes in region i. The arrow indicates the growth direction of the NT. **f**, The nanobeam electron diffraction patterns in regions i–vi

marked by the dashed rectangles in **e**. Indices [*hkl*] denote the zone axis of the NT, starting near [$12\bar{1}$] and showing a progressive twist of the lattice along the NT. The dashed triangles consist of the three diffraction points with the same spatial relationship in the diffraction pattern, highlighting the rotation of the (101) and (012) planes from 1-6. **g**, A schematic displaying the rotation of the NT along the growth direction; the insets present the crystal structures in three different zones along the NT. d, L, and Θ_{CA} represent the diameter, length, and chiral angle of the WS2 NT, respectively. **h**, Scatter plot of the twist per unit length in WS₂ NTs with different chiral angles. Error bars represent one standard deviation from calculating rotation angles using the diffraction data.

diameter, the interlayer spacing displays a linear decrease in the armchair and zigzag WS₂ NTs (Fig. 4b). However, this linear relationship is not observed in the chiral WS₂ NTs with helical angles of $17 \pm 0.5°$, likely due to the handedness of the chiral WS₂ NTs. Furthermore, there is also no simple relation in the M-CA WS₂ NTs (Fig. 4c).

Faceting and helicity are two typical characteristics of multi-walled NTs that have been observed and theoretically modelled in boron nitride NTs and carbon NTs[36–39]. In our analysis, we find remarkable circumferential faceting and helicity along the vertical-grown multi-walled WS₂ NTs. The circumferential faceting, which results in the polygonal cross-sections of multi-walled WS₂ NTs (Fig. 4d and Supplementary Fig. 36a–d), exists if the tube diameter is larger than

a critical value (Supplementary Fig. 36e–g)[36,40–42]. The surface structures of the faceted TMD NTs are uncovered by aberration-corrected high-angle ADF-STEM imaging, in which the distribution of the vertices with a bright contrast is identified along the tube (Supplementary Figs. 37–40). A comparison of the STEM images (Supplementary Figs. 37, 38 and 41a,b) clearly shows that the axial facets appear only in the chiral multi-walled WS₂ NTs, not in the achiral ones. This is in agreement with previous theoretical studies in double-walled carbon and boron nitride nanotubes[36]. For multi-chiral WS₂ NTs, the STEM studies reveal that a cross-sectional polygonalization occurs when the shells with different chirality have special helical angles matching[40,43]. For example, the faceting characteristics of multi-walled bichiral WS₂ NTs with a mixture
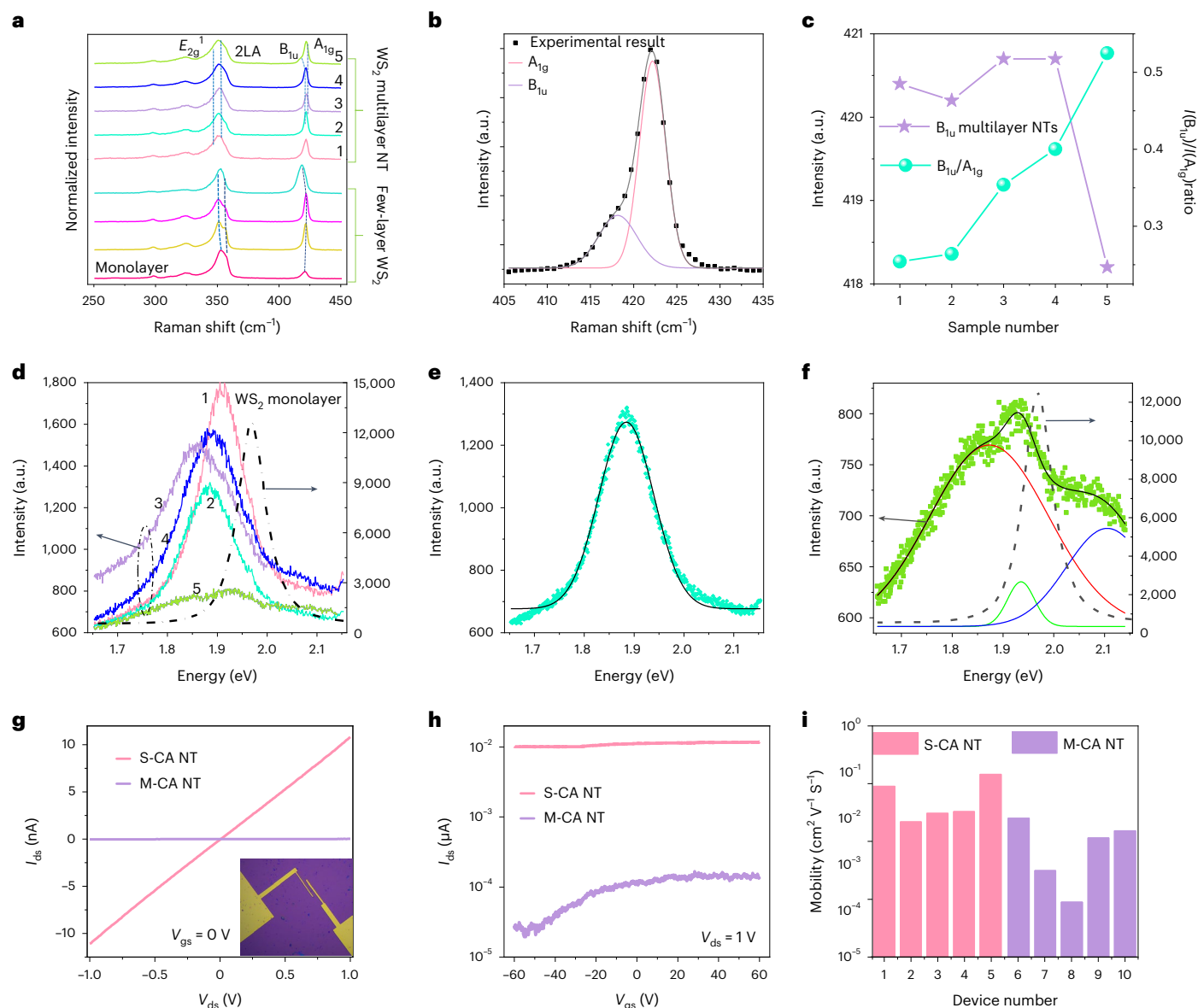
Fig. 5 | Optical and electronic characterizations of WS$_2$ multi-walled NTs.
a, Raman spectra of multilayer WS$_2$ NTs grown at ~835–840 °C, compared with those of the monolayer and few-layer WS$_2$ crystals. **b**, Lorentz fitting of the Raman spectrum of the WS$_2$ multi-walled NTs. The energy of the B$_{1u}$ mode is lower than the A$_{1g}$ mode. **c**, Raman shift of the B$_{1u}$ mode and the intensity ratio of the B$_{1u}$ and A$_{1g}$ modes ($I(B_{1u})/I(A_{1g})$) for different NT samples. **d**, PL spectra of multilayer WS$_2$ NTs grown at ~835–840 °C. The left axis is for the coloured, numbered spectra, whereas the right axis is for the dashed line. **e,f**, The Lorentz fitting of the PL spectrum of samples 2 (**e**) and 5 (**f**). In **f**, the left axis is for the coloured points and lines, whereas the right axis is for the dashed line. **g**, Output characteristics of the S-CA NT and M-CA NT FETs at V_{gs} = 0 V; the inset is the optical image of WS$_2$ NT FETs, and the gold region represents the Cr/Au contact pads. **h**, Transfer characteristics of the S-CA NT and M-CA NT FETs at V_{ds} = 1 V. **i**, Statistical distribution of the output current at V_{ds} = 1 V and V_{gs} = 0 V, highlighting that the S-CA NT FETs show considerably higher conductance than the M-CA NT FETs.

of armchair and zigzag shells are in Supplementary Fig. 39, and those with similar (but not the same) chiral angles near 30° are in Supplementary Fig. 40. However, the facet formation is suppressed in the M-CA WS$_2$ NTs with different helical angles between the shells, resulting in a corrugated NT surface (Supplementary Figs. 41 and 42). Furthermore, the vertices can significantly enlarge the interlayer spacing and lead to an asymmetric lattice fringe around the tube and a non-uniform lattice fringe along the tube[36] (Supplementary Fig. 40).

The helicity characteristics are confirmed in the high-resolution images obtained by TEM and high-angle ADF-STEM, as well as nanobeam electron diffraction (Fig. 4e,f). For example, a WS$_2$ NT with multiple helical angles of 0.5 ± 0.5° shows lattice fringes with an in-plane lattice constant of 0.272 ± 0.002 nm in (101) planes that are

perpendicular to the axis of the tube. Figure 4f shows that the diffraction patterns rotate systematically away from the crystal orientation of [12$\bar{1}$] when the beam is displaced along the tube. The ($\bar{1}$11) planes remain perpendicular to the axis of the tube, but the (101) and (012) planes progressively rotate with a fixed helicity along the tube. A schematic diagram of the crystal structure along the tube is shown in Fig. 4g. Detailed measurements demonstrate that the NT rotates by approximately 31.0° over a distance of 125 nm along the tube, and the helicity results in an obvious screw dislocation of the lattice fringes (Supplementary Fig. 43). Similarly, the diffraction data for various S-CA (chiral or achiral) and M-CA NTs (Fig. 4h) show the following: (1) the S-CA NTs have nearly axial symmetry without helicity; and (2) the M-CA WS$_2$ NTs have multiple chiral angles distributed in a small range (for example,

within 0.5 ± 0.5° or 29.5 ± 0.5°), and display an apparent rotation of helicity; while (3) the multi-walled bichiral WS$_2$ NTs with mixed armchair and zigzag shells have axial symmetry without helicity.

Vibrational, optical and electronic characterizations

Micro-Raman spectra of the WS$_2$ multi-walled NTs grown at ~835–840 °C reveal distinct features in comparison to monolayer and few-layer WS$_2$ crystals (Fig. 5a and Supplementary Fig. 44a,b). Notably, the vibration modes in WS$_2$ multi-walled NTs are independent of their layer numbers, in contrast to the monolayer and few-layer WS$_2$ crystals. Additionally, the B$_{1u}$ mode resulting from the curvature and structural disorder inherent in a NT[8] is observed with an energy lower than the A$_{1g}$ mode (Fig. 5b). The decrease of diameters of the NTs among the samples from 1 to 5 (the structural analysis is in Supplementary Fig. 44c) results in a linear-like dependence of the intensity ratio $I(B_{1u})/I(A_{1g})$ for samples (Fig. 5c). However, the Raman shift of the B$_{1u}$ mode is independent of the diameters (Fig. 5c), indicating that the B$_{1u}$ mode is not solely determined by the curvature but also by other structural properties, such as the strong mechanical coupling between the van der Waals–coupled single-walled NTs[44].

Photoluminescence (PL) spectra of the WS$_2$ multi-walled NTs (Fig. 5d) show a dramatically decreased quantum efficiency compared to the WS$_2$ monolayer (also Supplementary Fig. 43d). The PL spectra of four samples (1–4) can be fitted by Lorentzian functions (Fig. 5e and Supplementary Fig. 45), with the prominent symmetric peak around 1.86–1.91 eV originating from the A exciton[45,46]. However, the PL spectrum of sample 5 (Fig. 5e) displays different features. First, the PL intensity is notably lower; second, the PL curve is composed of multiple transition peaks located at 1.87 and 2.11 eV (Fig. 5f), identified as the A and B excitons, respectively[45,46]. Third, the peak located at 1.94 eV has a lower intensity compared to the A and B excitons, and intriguingly displays similarities to an interlayer exciton transition in twisted WS$_2$ bilayers[47]. Supplementary Figs. 46 and 47 indeed demonstrate that the relative orientations of the shells in the synthesized WS$_2$ multi-walled NTs would result in a 1D moiré pattern. These special PL features in sample 5 are more common in WS$_2$ multi-walled NTs grown at ~840–845 °C (Supplementary Fig. 48). The S-CA and M-CA multi-walled NTs, corresponding to the 'roll-up' of untwisted and twisted WS$_2$ multilayers, respectively, display distinct optical properties of 1D TMD structures, as confirmed by the further measurements of their reflection spectra (Supplementary Fig. 49). Similarly, the Raman and PL properties of the synthesized WSe$_2$ NTs are studied in Supplementary Fig. 50.

First-principles calculations using density functional theory were performed to investigate the electronic band structures of the S-CA and M-CA WS$_2$ multi-walled NTs (Supplementary Section 5). The results indicate that the energy gap in the WS$_2$ NTs is significantly smaller compared to their 2D counterparts due to the increased curvature and stronger interlayer interactions (Supplementary Fig. 52 and Supplementary Table 3)[48–50]. This sheds light on the shrinkage of the A- and B-exciton transitions that appeared in the S-CA and M-CA WS$_2$ NTs. Notably, the reduction in the energy gap is more prominent in M-CA rather than in S-CA WS$_2$ NTs (Supplementary Figs. 53 and 54 and Supplementary Table 4), highlighting the stronger interlayer interactions induced by the twist. Moreover, we theoretically reveal that the bandgap is indirect in armchair NTs, but direct in zigzag NTs (Supplementary Fig. 53), which is consistent with previous calculations in MoS$_2$ NTs[48,50].

To investigate the electrical transport properties of the synthesized NTs, we fabricated field-effect transistors (FETs) on the SiO$_2$/Si substrate using the WS$_2$ multi-walled NTs grown at ~835–840 °C and ~840–845 °C (inset of Fig. 5g and Supplementary Fig. 55a). At zero gate voltage, the output characteristics of the FETs, which depict drain–source current I_{ds} versus drain–source voltage V_{ds}, reveal that the multi-walled M-CA NT-based device exhibits little conduction, while that of the S-CA NT shows considerably higher conductance

with a current on the order of 10 nA at 1 V bias (Fig. 5g). The output characteristics under different gate–source voltages (V_{gs}) demonstrate n-type doping of the devices (Supplementary Fig. 56a), due to the electron concentration of the 'intrinsic' WS$_2$ NTs. The transfer characteristics (I_{ds}–V_{gs}) of the NT FETs (Fig. 5h) indicate a relatively small tunability, which is systematically studied in Supplementary Figs. 57–60. The electrical transport property can be improved by an annealing process, as demonstrated in Supplementary Figs. 61 and 62 and Supplementary Table 5.

Measurements of nearly 40 WS$_2$ NT FET devices confirm that the overall current of a S-CA NT device is approximately 2–4 orders of magnitude larger than that of a M-CA NT device at zero gate voltage (Fig. 5i and Supplementary Fig. 56b). Furthermore, the S-CA NT device exhibits a FET electron mobility that is approximately 1–3 orders of magnitude higher than that of the M-CA NT device (Supplementary Figs. 55b and 56c), highlighting the significantly higher conductivity in the multi-walled S-CA WS$_2$ NT. The ratio of the FET devices with higher output current and mobility is consistent with the percentage of NTs of single chiral angles grown at low and high growth temperatures, indicating differences in electrical performance in the S-CA and M-CA NTs because of their different chiral structures.

In conclusion, we have demonstrated a catalytic CVD method for preparing WS$_2$ and WSe$_2$ NTs using Au NPs as catalysts. The growth mechanisms and the role of Au NPs during the formation of TMD NTs at different temperatures are elucidated. The ability to synthesize TMD NTs with controllable chiral angles offers exciting possibilities to investigate the effect of chirality on their structural and physical properties, such as faceting and helicity vibrational modes, electronic band structures and carrier transport. Our approach has broad applicability for growing other TMD NTs with specific, customizable structures, enabling the rational tuning of their electronic band structures, light–matter interactions, spintronics, many-body excitons, carrier confinement or carrier separation. In addition, this strategy offers a potential strategy to further carefully control the chirality of TMD NTs, which is critical for both exploring single-chirality physics and realizing specific device functions. Our study thus greatly expands the TMD NT platform for both fundamental studies and technological applications.

Online content

Any methods, additional references, Nature Portfolio reporting summaries, source data, extended data, supplementary information, acknowledgements, peer review information; details of author contributions and competing interests; and statements of data and code availability are available at https://doi.org/10.1038/s41563-023-01590-5.

References

1. Xiang, R. et al. One-dimensional van der Waals heterostructures. *Science* **367**, 537–542 (2020).
2. Musfeldt, J. L., Iwasa, Y. & Tenne, R. Nanotubes from layered transition metal dichalcogenides. *Phys. Today* **73**, 42–48 (2020).
3. Tenne, R., Margulis, L., Genut, M. & Hodes, G. Polyhedral and cylindrical structures of tungsten disulphide. *Nature* **360**, 444–446 (1992).
4. Zhang, Y. J. et al. Enhanced intrinsic photovoltaic effect in tungsten disulfide nanotubes. *Nature* **570**, 349–353 (2019).
5. Qin, F. et al. Superconductivity in a chiral nanotube. *Nat. Commun.* **8**, 14465 (2017).
6. Goldbart, O. et al. Diameter-dependent wetting of tungsten disulfide nanotubes. *Proc. Natl Acad. Sci. USA* **113**, 13624–13629 (2016).
7. Kaplan-Ashiri, I. et al. On the mechanical behavior of WS$_2$ nanotubes under axial tension and compression. *Proc. Natl Acad. Sci. USA* **103**, 523–528 (2006).
8. Staiger, M. et al. Excitonic resonances in WS$_2$ nanotubes. *Phys. Rev. B* **86**, 165423 (2012).

9. Levi, R., Bitton, O., Leitus, G., Tenne, R. & Joselevich, E. Field-effect transistors based on WS$_2$ nanotubes with high current-carrying capacity. *Nano Lett.* **13**, 3736–3741 (2013).

10. Xia, H. et al. Probing the chiral domains and excitonic states in individual WS$_2$ tubes by second-harmonic generation. *Nano Lett.* **21**, 4937–4943 (2021).

11. Zak, A. et al. Scaling up of the WS$_2$ nanotubes synthesis. *Fuller. Nanotub. Carbon Nanostruct.* **19**, 18–26 (2010).

12. Feldman, Y., Wasserman, E., Srolovitz, D. J. & Tenne, R. High-rate, gas-phase growth of MoS$_2$ nested inorganic fullerenes and nanotubes. *Science* **267**, 222–225 (1995).

13. Kim, H. et al. Seed growth of tungsten diselenide nanotubes from tungsten oxides. *Small* **11**, 2192–2199 (2015).

14. Liu, Z. et al. WS$_2$ nanotubes, 2D nanomeshes, and 2D in-plane films through one single chemical vapor deposition route. *ACS Nano* **13**, 3896–3909 (2019).

15. Chithaiah, P. et al. Solving the "MoS$_2$ nanotubes" synthetic enigma and elucidating the route for their catalyst-free and scalable production. *ACS Nano* **14**, 3004–3016 (2020).

16. Qin, F. et al. Diameter-dependent superconductivity in individual WS$_2$ nanotubes. *Nano Lett.* **18**, 6789–6794 (2018).

17. Sinha, S. S. et al. Size-dependent control of exciton–polariton interactions in WS$_2$ nanotubes. *Small* **16**, e1904390 (2020).

18. Wang, X. H., Zheng, C. C. & Ning, J. Q. Influence of curvature strain and van der Waals force on the inter-layer vibration mode of WS$_2$ nanotubes: a confocal micro-Raman spectroscopic study. *Sci. Rep.* **6**, 33091 (2016).

19. Kim, S. Y., Kwak, J., Ciobanu, C. V. & Kwon, S. Y. Recent developments in controlled vapor-phase growth of 2D group 6 transition metal dichalcogenides. *Adv. Mater.* **31**, e1804939 (2019).

20. Li, H., Li, Y., Aljarb, A., Shi, Y. & Li, L. J. Epitaxial growth of two-dimensional layered transition-metal dichalcogenides: growth mechanism, controllability, and scalability. *Chem. Rev.* **118**, 6134–6150 (2018).

21. Deniz, H. & Qin, L.-C. Determination of the chiral indices of tungsten disulfide (WS$_2$) nanotubes by electron diffraction. *Chem. Phys. Lett.* **552**, 92–96 (2012).

22. Chen, Y., Deniz, H. & Qin, L. C. Accurate measurement of the chirality of WS$_2$ nanotubes. *Nanoscale* **9**, 7124–7134 (2017).

23. Remškar, M., Škraba, Z., Ballif, C., Sanjinés, R. & Lévy, F. Stabilization of the rhombohedral polytype in MoS$_2$ and WS$_2$ microtubes: TEM and AFM study. *Surf. Sci.* **433–435**, 637–641 (1999).

24. Houben, L. et al. Diffraction from disordered stacking sequences in MoS$_2$ and WS$_2$ fullerenes and nanotubes. *J. Phys. Chem. C* **116**, 24350–24357 (2012).

25. Magnin, Y., Amara, H., Ducastelle, F., Loiseau, A. & Bichara, C. Entropy-driven stability of chiral single-walled carbon nanotubes. *Science* **362**, 212–215 (2018).

26. Xu, Z., Bai, X., Wang, Z. L. & Wang, E. Multiwall carbon nanotubes made of monochirality graphite shells. *J. Am. Chem. Soc.* **128**, 1052–1053 (2006).

27. Guo, W. & Guo, Y. Energy optimum chiralities of multiwalled carbon nanotubes. *J. Am. Chem. Soc.* **129**, 2730–2731 (2007).

28. Jany, B. R. et al. Controlled growth of hexagonal gold nanostructures during thermally induced self-assembling on Ge(001) surface. *Sci. Rep.* **7**, 42420 (2017).

29. Jeon, S. et al. Reversible disorder-order transitions in atomic crystal nucleation. *Science* **371**, 498–503 (2021).

30. Zhao, B. et al. Synthetic control of two-dimensional NiTe$_2$ single crystals with highly uniform thickness distributions. *J. Am. Chem. Soc.* **140**, 14217–14223 (2018).

31. Li, B. et al. Van der Waals epitaxial growth of air-stable CrSe$_2$ nanosheets with thickness-tunable magnetic order. *Nat. Mater.* **20**, 818–825 (2021).

32. Cui, X. et al. Rolling up transition metal dichalcogenide nanoscrolls via one drop of ethanol. *Nat. Commun.* **9**, 1301 (2018).

33. Zhao, B. et al. High-order superlattices by rolling up van der Waals heterostructures. *Nature* **591**, 385–390 (2021).

34. DiStefano, J. G. et al. Nanoparticle@MoS$_2$ core–shell architecture: role of the core material. *Chem. Mater.* **30**, 4675–4682 (2018).

35. Lavie, A. et al. Synthesis of core–shell single-layer MoS$_2$ sheathing gold nanoparticles, AuNP@1L-MoS$_2$. *Nanotechnology* **28**, 24LT03 (2017).

36. Leven, I., Guerra, R., Vanossi, A., Tosatti, E. & Hod, O. Multiwalled nanotube faceting unravelled. *Nat. Nanotechnol.* **11**, 1082–1086 (2016).

37. Guerra, R., Leven, I., Vanossi, A., Hod, O. & Tosatti, E. Smallest Archimedean Screw: facet dynamics and friction in multiwalled nanotubes. *Nano Lett.* **17**, 5321–5328 (2017).

38. Golberg, D., Mitome, M., Bando, Y., Tang, C. C. & Zhi, C. Y. Multi-walled boron nitride nanotubes composed of diverse cross-section and helix type shells. *Appl. Phys. A* **88**, 347–352 (2007).

39. Palser, A. H. R. Interlayer interactions in graphite and carbon nanotubes. *Phys. Chem. Chem. Phys.* **1**, 4459–4464 (1999).

40. Bandura, A. V., Lukyanov, S. I., Kuruch, D. D. & Evarestov, R. A. Multi-walled MoS$_2$ nanotubes. First principles and molecular mechanics computer simulation. *Phys. E* **124**, 114183 (2020).

41. Srolovitz, D. J., Safran, S. A., Homyonfer, M. & Tenne, R. Morphology of nested fullerenes. *Phys. Rev. Lett.* **74**, 1779–1782 (1995).

42. Garel, J. et al. Ultrahigh torsional stiffness and strength of boron nitride nanotubes. *Nano Lett.* **12**, 6347–6352 (2012).

43. Kolmogorov, A. N. & Crespi, V. H. Smoothest bearings: interlayer sliding in multiwalled carbon nanotubes. *Phys. Rev. Lett.* **85**, 4727–4730 (2000).

44. Gordeev, G., Wasserroth, S., Li, H., Flavel, B. & Reich, S. Moire-induced vibrational coupling in double-walled carbon nanotubes. *Nano Lett.* **21**, 6732–6739 (2021).

45. Yadgarov, L. et al. Strong light–matter interaction in tungsten disulfide nanotubes. *Phys. Chem. Chem. Phys.* **20**, 20812–20820 (2018).

46. Zeng, Z. et al. Controlled vapor growth and nonlinear optical applications of large-area 3R phase WS$_2$ and WSe$_2$ atomic layers. *Adv. Funct. Mater.* **29**, 1806874 (2019).

47. Zheng, S. et al. Coupling and interlayer exciton in twist-stacked WS$_2$ bilayers. *Adv. Opt. Mater.* **3**, 1600–1605 (2015).

48. Seifert, G., Terrones, H., Terrones, M., Jungnickel, G. & Frauenheim, T. Structure and electronic properties of MoS$_2$ nanotubes. *Phys. Rev. Lett.* **85**, 146–149 (2000).

49. Frey, G. L., Elani, S., Homyonfer, M., Feldman, Y. & Tenne, R. Optical-absorption spectra of inorganic fullerenelike MS_2 (M=Mo, W). *Phys. Rev. B* **57**, 6666–6671 (1998).

50. Zibouche, N., Kuc, A. & Heine, T. From layers to nanotubes: transition metal disulfides TMS$_2$. *Eur. Phys. J. B* **85**, 49 (2012).

Methods

Sample preparation

The TMD NTs were grown in a one-zone tube furnace. The WO$_3$ powder (99.99%; Alfa Aesar) was placed in a quartz boat at the central heating area of the high-temperature furnace, while the S or Se powder (99.999%; Alfa Aesar) in a quartz boat was located 40 cm away from the furnace, to ensure the negligible evaporation of S or Se powder during the evaporation of WO$_3$ powder. A Si substrate rinsed with acetone, alcohol and deionized water was predeposited by an ~10 nm Au catalyst layer by radio frequency magnetron sputtering. Then, the Au catalyst layer was annealed at 750 °C for 10 min to form 3D catalyst islands. The Si substrate with Au NPs was placed downstream (~30 cm) of the high-temperature furnace to trigger the nucleation of TMD NTs in a thermal CVD process. A vacuum pump can suck the gas into the reaction chamber and create a low-pressure environment. Each of the quartz tube sides was equipped with a gas inlet or outlet. The inlet gas flow of argon and hydrogen and the outlet gas flow were controlled by the angle-style valves at the two ends of the quartz tube to keep the pressure at a required value. Before heating, the system was purged with 1,215 standard cubic centimetres per minute (sccm) Ar (~99.999%) for 5 min to eliminate oxygen and moisture in the furnace. Then, the pressure in the tube was decreased and maintained at 850–950 mbar during the reaction process.

With the temperature increase in the furnace, the source material WO$_3$ powder was evaporated first and transformed by Ar gas on the surface of the Au catalyst NPs under low-pressure conditions. When the furnace temperature reached 800 °C, hydrogen gas was introduced into the reaction system. As the temperature of the furnace increased further to the required reaction value (980 °C), the S or Se powder was moved quickly towards the furnace by moving a magnet to attract an iron rectangle beside the boat containing the S or Se powder. The S or Se powder then started to evaporate and participate in the nucleation on the surface of the Au NPs. During this CVD reaction, the Ar gas at 200 sccm transported the precursors' vapour to the downstream growth substrate. When the growth was completed, a 500 sccm flow of Ar was introduced into the furnace to remove the residual reactants. The growth samples were obtained after the furnace was naturally cooled to ambient temperature.

Device fabrication and characterization

The synthesized WS$_2$ NTs were redispersed and uniformly dispersed in ethanol by an ultrasonic treatment for further processing. Then, ethanolic WS$_2$ NTs were dispersed onto the SiO$_2$/Si substrate, spin-coated with polymethyl methacrylate and fabricated by electron-beam lithography, followed by deposition of Cr/Au (10 nm Cr/50 nm Au), Ti/Au (5 nm Cr/50 nm Au) or Ni/Au (10 nm Cr/50 nm Au) for the electrical contacts. The electrical performance of the fabricated FETs was measured with a Lake Shore TTPX probe station and an Agilent B1500A semiconductor parameter analyser. The carrier mobility of the synthesized WS$_2$ NT and WS$_2$ nanosheet was calculated as $\mu_{1D} = \frac{L^2}{V_{ds}C_{1D}} \frac{dI_{ds}}{dV_{gs}}$ and $\mu_{2D} = \frac{L}{WV_{ds}C_{2D}} \frac{dI_{ds}}{dV_{gs}}$, respectively, where L is the channel length (indicated in Fig. 3a)[37]; W is the channel width of the nanosheet; and C_{1D} and C_{2D} are the capacitances of 1D NTs and 2D nanosheets, which were calculated as $C_{1D} = \frac{2\pi\varepsilon\varepsilon_0 L}{\cosh^{-1}[(r+t_{ox})/r]}$ and $C_{2D} = \frac{\varepsilon\varepsilon_0}{t_{ox}}$, where ε is the dielectric constant of SiO$_2$, ε_0 is the vacuum permittivity, t_{ox} is the thickness of SiO$_2$ and r is the radius of the synthesized NT. The carrier concentration of the WS$_2$ NT and WS$_2$ nanosheet was calculated as $n = C/q \times (V_g - V_t)$, where V_g is the gate voltage, V_t is the threshold voltage, C is the capacitance of 1D NT (C1D) and q is the charge of an electron.

STEM simulation

STEM image simulations were performed using the package QSTEM (http://www.qstem.org), which is based on the multi-slice algorithm. The simulation parameters were roughly the same for all crystals,

including the thermal diffuse scattering within the frozen phonon approximation. An 80 × 80 pixel area and a probe array of a 400 × 400 pixel area were employed. Box mode with a size of 60 Å × 60 Å × 100 Å ($x \times y \times z$) was used, and the zone axes were reached by the sample tilt function. In total, there were 100 slices along the zone axes, and each was one angstrom thick (50 slices with each being two angstroms thick for WS$_2$). The defocus, astigmatism and spherical aberration C3 were all set to zero in order to get the closest representation of the real structure. The inner and outer angles were 42° and 180° (for detector 1) and 7.8° and 16° (for detector 2), respectively, consistent with the experimental parameters.

Image processing

Raw STEM images were filtered using the winner filter and ABSF filter realized by Digital Micrograph (https://www.gatan.com/).

Author contributions

Q.A. conceived the original idea for the project. Q.A. developed the catalytic CVD method to prepare WS$_2$ and WSe$_2$ NTs and analysed the growth mechanisms. Q.A. performed the SEM, TEM and STEM characterizations and analysed all the experimental data. Q.A. carried out the Raman and PL characterizations and performed the FET device fabrications. W.X., P.L. and S.Y. performed first-principles calculations and provided theoretical support. Q.A. and S.H. carried out the electrical characterizations. Q.A. and S.Y. wrote the paper. F.H. and Y.Y. discussed the results and provided suggestions during the process of draughting. Q.A., S.Y., Y.Y. and F.H. revised the manuscript. X.H. made some suggestions during the FET device fabrication. All authors commented on the manuscript.

Competing interests

The authors declare no competing interests.

Additional information

Supplementary information The online version contains supplementary material available at https://doi.org/10.1038/s41563-023-01590-5.

Correspondence and requests for materials should be addressed to Qinwei An or Shengjun Yuan.

Peer review information *Nature Materials* thanks Jeremy Sloan, Zheng Liu and the other, anonymous, reviewer(s) for their contribution to the peer review of this work.

Reprints and permissions information is available at www.nature.com/reprints.